The application of encoder–decoder neural networks in high accuracy and efficiency slit-scan emittance measurements

Ma, S.; Arnold, A.; Michel, P.; Murcek, P.; Ryzhov, A.; Schaber, J.; Steinbrück, R.; Evtushenko, P.; Teichert, J.; Hillert, W.; Xiang, R.; Zhu, J.;

Originally published:

February 2023

Nuclear Instruments and Methods in Physics Research A 1050(2023), 168125

DOI: https://doi.org/10.1016/j.nima.2023.168125

The application of encoder-decoder neural networks in high accuracy and efficiency slit-scan emittance measurements

S. Ma,[1,2,†] A. Arnold,[1] P. Michel,[1] P. Murcek,[1] A. Ryzhov,[1] J. Schaber,[1] R. Steinbrück,[1] P. Evtushenko,[1] J. Teichert,[1,*] W. Hillert,[2,3] R. Xiang,[1] and J. Zhu[3]

1. Helmholtz-Zentrum Dresden-Rossendorf, 01328 Dresden, Germany

2. Universität Hamburg, 20148 Hamburg, Germany

3. Deutsches Elektronen-Synchrotron (DESY), 22607 Hamburg, Germany.

Abstract

A superconducting radio-frequency (SRF) photo injector is in operation at the electron linac for beams with high brilliance and low emittance (ELBE) radiation center and generates continuous wave (CW) electron beams with high average current and high brightness for user operation since 2018. The speed of emittance measurement at the SRF gun beamline can be increased by improving the slit-scan system, thus the measurement time for one phase space mapping can be shortened from about 15 minutes to 90 seconds. The convolution neural networks are applied to improve the efficiency and accuracy of beamlet images processing. In order to estimate the uncertainty in the calculation of normalized emittance, we analyze the main error contributions.

1. Introduction

High gradient radio-frequency photoelectron injectors (rf guns) are a kind of best candidates to generate electron beams with low emittance, high brightness, and ultrashort bunches of pico- to sub-picoseconds at present [1]. The remarkable high beam quality of these electron injectors has opened up new development of modern accelerator-based scientific facilities, such as extreme ultraviolet (XUV) [2,3] and X-ray free-electron lasers (X-FEL) [4], energy recovery linacs (ERL) [5], MeV ultrafast electron diffraction (UED) [6], and hadron-beam cooling [7].

One of the most critical parameters characterizing rf guns is the transverse emittance. Originally, the transverse emittance is defined as the projected area occupied by the beam particles on the two-dimensional phase space [8, 9] at a given position z along the beam axis. The area calculation is difficult for particle distributions with vaguely defined boundaries, and it requires further specifications. An alternative and widely used way to overcome this difficulty is to adopt the concept of root-mean-square (RMS) emittance based on the second moments of the particle distribution, proposed by Lapostolle [10] and Sacherer [11].

† Corresponding author: s.ma@hzdr.de;
* j.teichert@hzdr.de.

How to measure the transverse emittance with high accuracy and speed is always an important question, especially at a user facility where the time slot for the beam diagnostics is limited, and the task should be routinely done by the shift staff. Several measurement methods are popular at most facilities, for instance, multi-screen method [12], quadrupole or solenoid scan [13], beam tomography [14], slit-scan and pepper-pot [15]. An essential factor for selecting a suitable method is based on whether the beam is emittance or space-charge dominated. A criterion is defined in ref. [16]. For the low energy, high brightness beams from photo injectors, the space charge contributes so considerably that such methods like slit-scan or pepper-pot methods should be applied.

At the electron linac for beams with high brilliance and low emittance (ELBE) radiation center [17], a superconducting radio-frequency (SRF) gun has been developed and operated as an injector for the ELBE electron accelerator since 2007 [18]. At present, the SRF gun of second generation is working, referred to as SRF gun-II. It includes a 3.5-cell 1.3-GHz superconducting niobium cavity, a superconducting solenoid, and a photocathode with a corresponding laser system. A cathode supporting system cooled with liquid nitrogen (LN_2) allows the operation of normal-conducting photocathodes with a high quantum efficiency (QE). The SRF gun operates in continuous wave (CW) mode with a repetition rate up to 13 MHz. A diagnostics beamline allows the detailed characterization of the electron beam and the further optimization of the SRF gun's operation.

To meet the requirement of emittance measurement in our user facility, i.e. speediness and accuracy, we upgraded the slit-scan setup in the diagnostic beamline. The ultra-high-vacuum (UHV) translation stage for the slit movement, drive motors, and control units have been replaced by advanced systems. The slit moving velocity with the new motor is now adjustable from 0 to 25 mm/s. The new control software has been developed, and the data analysis methods have been improved meanwhile. The old beamlet images processing method we used was based on 2D: first to use Gaussian fitting or set a threshold value to distinguish the beamlet and noise images; second to filter and sum all beamlet images and scale the region-of-interest (ROI) manually to avoid the influence from outside noise; third to calculate the emittance. However, all the critical information for the phase space reconstruction and emittance calculation is the beamlet projection profile in one dimension. Considering that machine learning (ML) has become one of the most widely used and successfully developed method in image processing [19], the benefits expected here for the data analysis of the slit-scan measurement are an increase in speed, a higher accuracy of the beamlet profile, and the omission of manual intervention during the image data processing.

In the first part of this paper, the theory of the slit-scan emittance measurement method is briefly reviewed. The second part describes the emittance measurement system in the SRF gun beamline. The third part introduces two convolutional neural networks (CNN) [19-21], whereby one is for beamlet images classification, and the other one, named encoder-decoder CNN, is for image noise reduction. The measurement error of the slit-scan process is discussed and analysed in the fourth part. Computer simulation of the slit-scan method based on the ASTRA code [22] is applied for the analysis in this part. The following fifth part presents our emittance measurement results with the new slit-scan system. The preciseness of the new measurement system is confirmed by comparing the experimental results with ASTRA beam dynamics simulation. The conclusions are given in the last part.

2. Slit-scan technique

2.1. Emittance measurement

The slit-scan and multi-slit techniques are widely used for measuring the transverse phase space and transverse projected emittance of high brightness electron beams produced by photo injectors. In these methods, the space charge dominated beam is split into many small and emittance dominated beamlets using a mask with one or several narrow slits. The particles of the beamlets drift from the mask position to a screen, as shown in Fig. 1. The data analysis works in the same way for single-slit scan as for multi-slit scan method. In both cases the particle divergence at slit position is transferred to a position distribution on the screen.

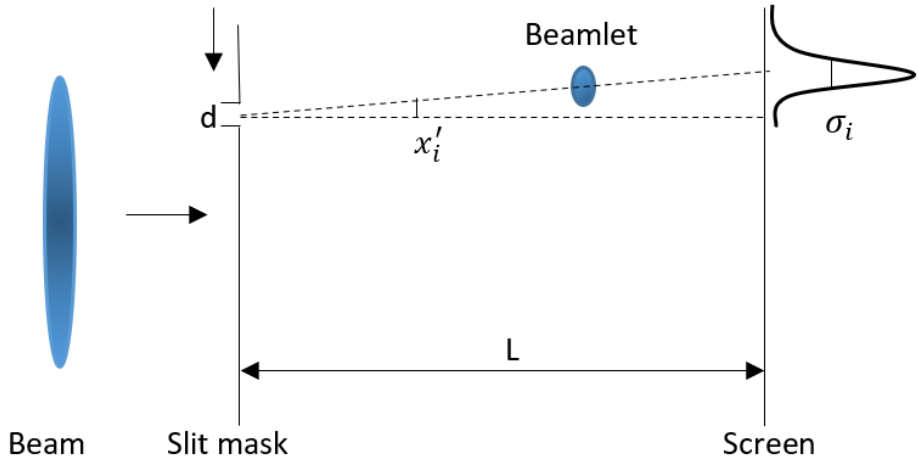

FIG. 1. Illustration of single-slit scan emittance measurement scheme.

For the beamlets a linear beam transport between the slit mask is assumed and thus the observation screen can be described by the transport matrix

$$\begin{pmatrix} x_{screen} \\ x'_{screen} \end{pmatrix} = \begin{pmatrix} 1 & L \\ 0 & 1 \end{pmatrix} \begin{pmatrix} x_{slit} \\ x'_{slit} \end{pmatrix}. \quad (1)$$

The RMS transverse emittance ε is defined as

$$\varepsilon = \sqrt{\langle x^2 \rangle \langle x'^2 \rangle - \langle xx' \rangle^2} \ , \quad (2)$$

and a normalized transverse emittance ε_n can be written as

$$\varepsilon_n = \frac{p_z}{m_0 c} \sqrt{\langle x^2 \rangle \langle x'^2 \rangle - \langle xx' \rangle^2}. \quad (3)$$

Here the second moments $\langle x^2 \rangle$, $\langle x'^2 \rangle$, $\langle xx' \rangle$ are given based on the particle distribution $\rho(x, x')$:

$$\langle x^2 \rangle = \int \rho \cdot (x - \langle x \rangle)^2 dx dx', \langle x'^2 \rangle = \int \rho \cdot (x' - \langle x' \rangle)^2 dx dx',$$

$$\langle xx' \rangle = \int \rho \cdot (x - \langle x \rangle)(x' - \langle x' \rangle) dx dx', x' = \frac{p_x}{p_z} \ , \quad (4)$$

where p_x is the horizontal beam momentum, p_z is the longitudinal beam momentum and it is approximately equal to the beam momentum, m_0 is the rest mass of electron, and c is the speed of light. In the slit-scan case, the $\langle \ \ \rangle$ is related to the averaging over the beamlets with the weight n_i, which are the particle intensities through the slit at i-th position. The bunch center at the slit plane is $\langle x \rangle = \frac{\sum n_i x_{si}}{\sum n_i}$, and x_{si} is the slit coordinate at i-th position. The beam size at the slit plane is $\langle x^2 \rangle = \frac{\sum n_i (x_{si} - \langle x \rangle)^2}{\sum n_i}$. The term $\langle x' \rangle = \frac{\sum n_i \overline{x'}_i}{\sum n_i}$ is the mean slope of the bunch with $\overline{x'}_i = \frac{\overline{x}_{sci} - x_{si}}{L}$. Here $\overline{x}_{sci}$ is the position of the i-th beamlet center on the screen, and L is the drift distance. The i-th beamlet divergence is $\sigma_i'^2 = \frac{\sigma_i^2 - \frac{d^2}{12}}{L^2}$, where σ_i is the i-th beamlet RMS size measured on the screen, d is the slit size and the factor 1/12 is from the RMS value of the slit. The quantities in Eq. (3) can now be expressed by values measured at the screen:

$$\langle x'^2 \rangle = \frac{\sum \left[n_i \sigma_i'^2 + n_i (\overline{x'}_i - \langle x' \rangle)^2 \right]}{\sum n_i} \ , \quad (5)$$

$$\langle xx' \rangle = \frac{\sum n_i x_{si} \overline{x'}_i}{\sum n_i} \ . \quad (6)$$

2.2. Fast slit-scan measurement system at ELBE

The slit-scan system is a part of the diagnostics beamline, as shown in Fig. 2 [18]. The whole system is located at screen-station 2 and 3. Station 2 includes one single-slit mask with a 100 µm wide slit, one yttrium aluminum garnet (YAG) screen, and one calibration screen. Station 3 has one YAG screen, one optical transition radiation (OTR) screen, and one calibration screen (see Fig. 3). An encoder system delivers the actual slit position, and a second actuator serves for slit tilting with respect to the beam axis. Motor drivers and encoder electronics are made by Phytron GmbH. The distance between the slit mask and the YAG screen in screen-station 3 is 0.75 m. For image recording a 12-bit CCD camera Basler Scout with 659 x 494 pixels is used.

The corresponding size of one pixel on the screen is 25.3 μm. The control software is written in LabView and runs on a standard PC.

In the control software, the camera loop and the slit movement loop run in parallel, as shown in Fig. 4. The beamlet images are captured while the slit is continuously moving. In the i-th loop, the slit position P_{ci} is recorded, typically at 10 Hz depending on the macro pulse trigger which indicates that beam is on. At the same time T_{ci}, a command is sent to the camera to capture one image. During the camera exposure, the recording time is T_{ri}. The camera exposure time is usually chosen as long as the macro pulse length to cover the full pulse and to reduce the background noise from the dark current. Taking the aforementioned into account, the exact position of the slit when the camera captures the image can be written as

$$P_{r_i} = \frac{P_{c_{i+1}} - P_{c_i}}{T_{c_{i+1}} - T_{c_i}} \cdot \left(T_{r_i} - T_{c_i}\right) + P_{c_i}. \tag{7}$$

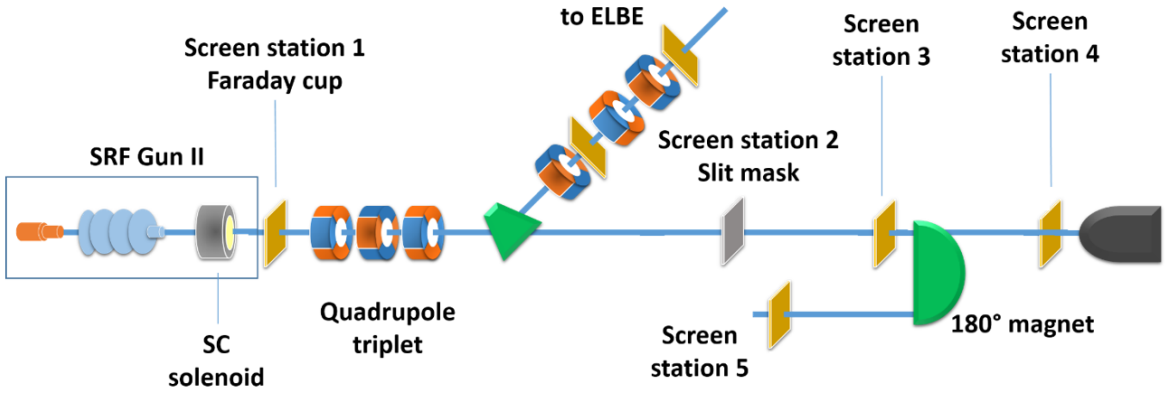

FIG. 2. The diagnostic beamline of ELBE SRF Gun II.

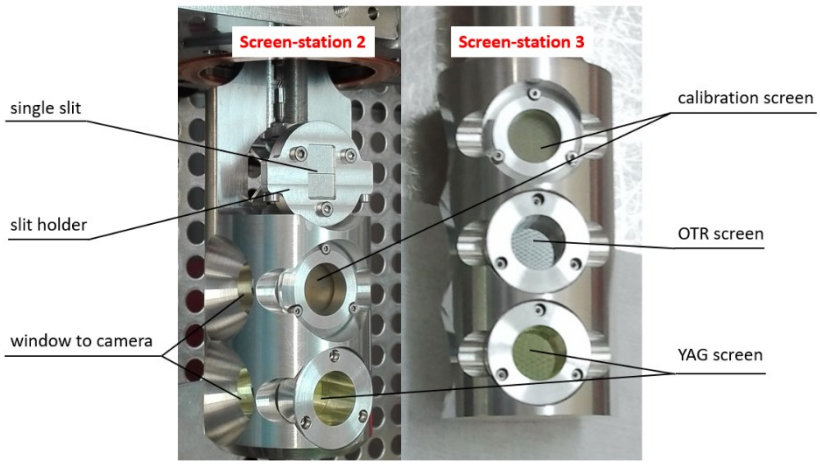

FIG. 3. Photographs of screen-station 2 and screen-station 3.

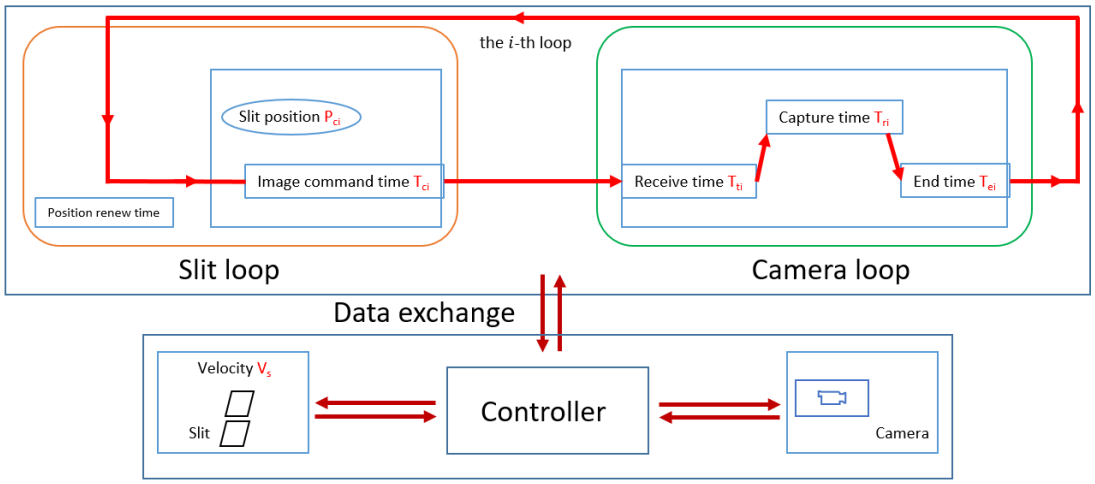

FIG. 4. Single-slit scan control system scheme.

3. Image processing based on Machine Learning

The first ML data processing step uses a CNN for image classification to eliminate datasets of needless images which contain no beamlet information. The input of the neural network is the horizontal projection of the beamlet images, which is a 1D intensity array with 494 values. The neural network structure is shown in Fig. 5 and consists of two convolution layers, where one pooling layer, and a fully-connected layer with two nodes as the output layer. The output is a one-hot encoding to determine the processing image is useful for further treatment.

The second image processing step is mainly intended for noise elimination. The input data is the 1D intensity array of the reduced number of beamlet image datasets selected in the first step. The output should be a nearly perfectly reconstructed beamlet intensity profile without noise and other artifacts. For that purpose, an encoder-decoder network is suitable [19]. The encoder-decoder consists of two parts, the encoder and the decoder. For the encoder part, the input is the data $x \in R^m$ and the output is the reconstructed data $y \in R^n$. One of the hidden layers stores the data features, written as the latent space h_k. The network has to learn the functions $f_e: R^m \rightarrow R^k$ and $f_d: R^k \rightarrow R^n$. In principle, the features of the input data will be learnt and stored into the latent space, then the decoder layers will rebuild the signal as the output from the latent space. The specific structure of the encoder-decoder network used in this paper is presented in Fig. 6.

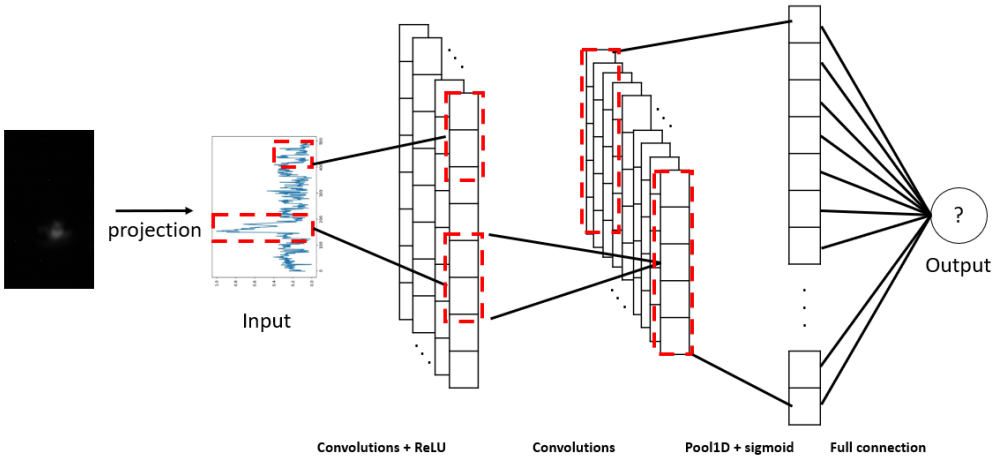

FIG. 5. Beamlet images classification network. The input data is a one-dimension signal with the beamlet intensity horizontal projection. The first convolution layer outputs 32 features with a leaky rectified-linear-unit (ReLU) function. The second convolution layer outputs 64 features. After this, a pooling layer and sigmoid function are used. The fully-connected layer is in the end and the log-softmax function scales the value from 0 to 1. The output value will be 1 when the log-softmax value between 0.5 and 1, and will be 0 otherwise.

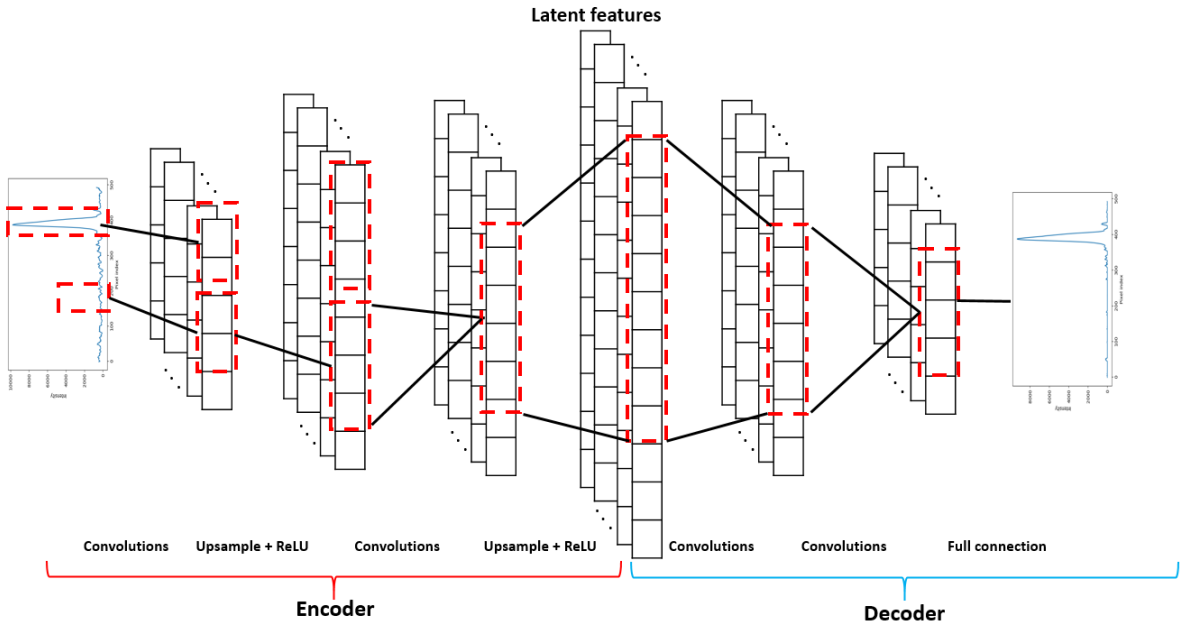

FIG. 6. The encoder-decoder network structures. The input data is the same as the classification network. The output features of the convolution layers in the encoder part are 16 and 32 with stride 1. The upsample layers are both nearest and scaling factors are 2. The latent features are 982. The output features of the convolution layers in the decoder part are 32 and 16 with stride 2. In the end is a full connected layer. The kernel sizes used are all 3. The total number of parameters is 2 005 887.

The ML networks have to be trained and tested. For the image classification network, 2500 projection datasets from beamlet images were used, which were taken from experimental slit-scan measurements. Thereby 2000 were utilized for training and 500 for testing. The training applies the stochastic gradient descent method with the cross-entropy [23] as a loss function.

The final accuracy obtained from the test data is 98.8%. For the encoder-decoder network, the training data came from 1502 experimental beamlet images processed manually and through the median filter. Noise signal data was taken from 107 experimental images without beamlet signals. Based on these, a random combination of filtered beamlet and noise data was used to construct 167205 projection data records, of which, in turn 80% were used for training and 20% for testing. Fig. 7 illustrates four examples of the dataset. The training procedure was performed in the Maxwell Computer Cluster at DESY, using NVIDIA Tesla P100 GPU. The training time was about one and a half hours with one thousand epochs, 3072 batch size and mean square error (MSE) loss function. The optimizer used was Adam in Pytorch [24].

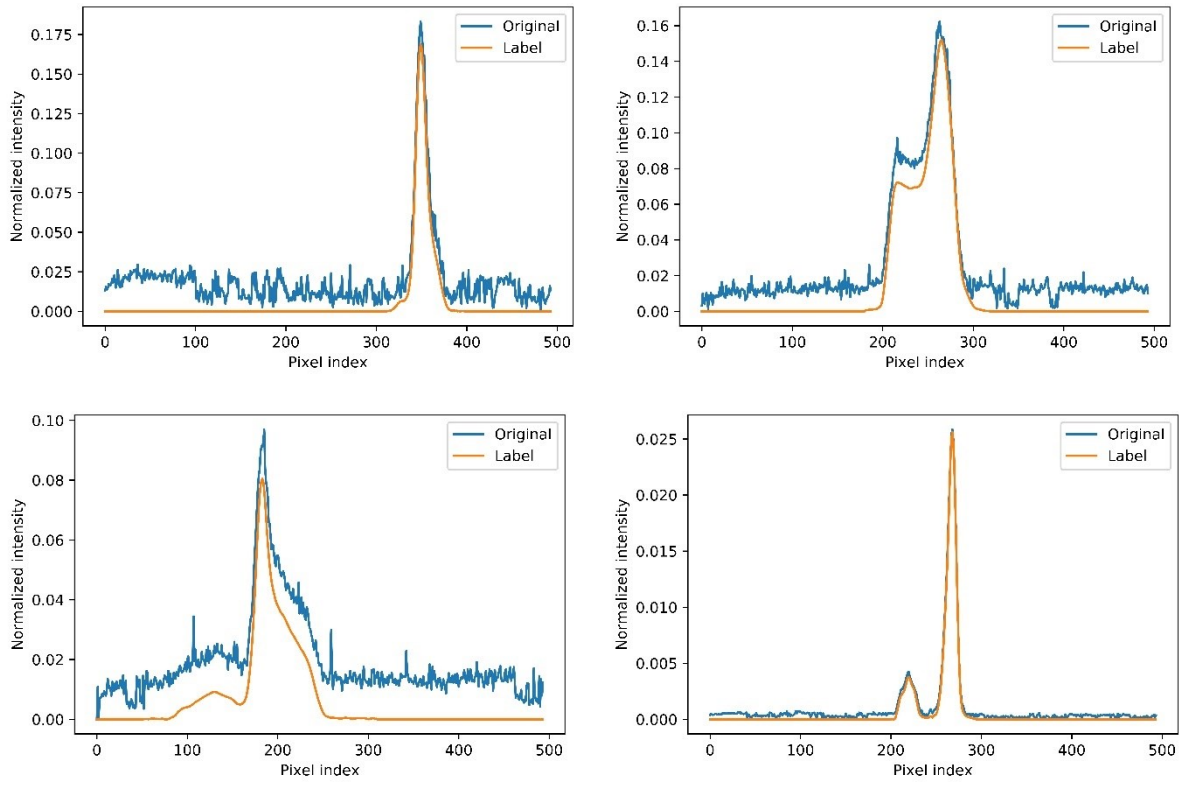

FIG. 7. The projection of beamlet images from simulation and the noise from the experiments.

Fig. 8 shows that the filter from machine learning (ML filter) has the potential to be more accurate than traditional filters, such as median and Butterworth filters. The true signal profile has two peaks with noise. The median and Butterworth filters can smooth the signal, but they are helpless to depress the noise to a low level. The Gaussian fitting method distorts the signal if it is beyond the Gaussian distribution. The advantage of the ML filter is, that it doesn't need to adjust the parameters for different beamlet images once the neural network is well trained and evaluated. The processing time for a single image is around 5 ms which is about one fourth of the traditional processing method we use before.

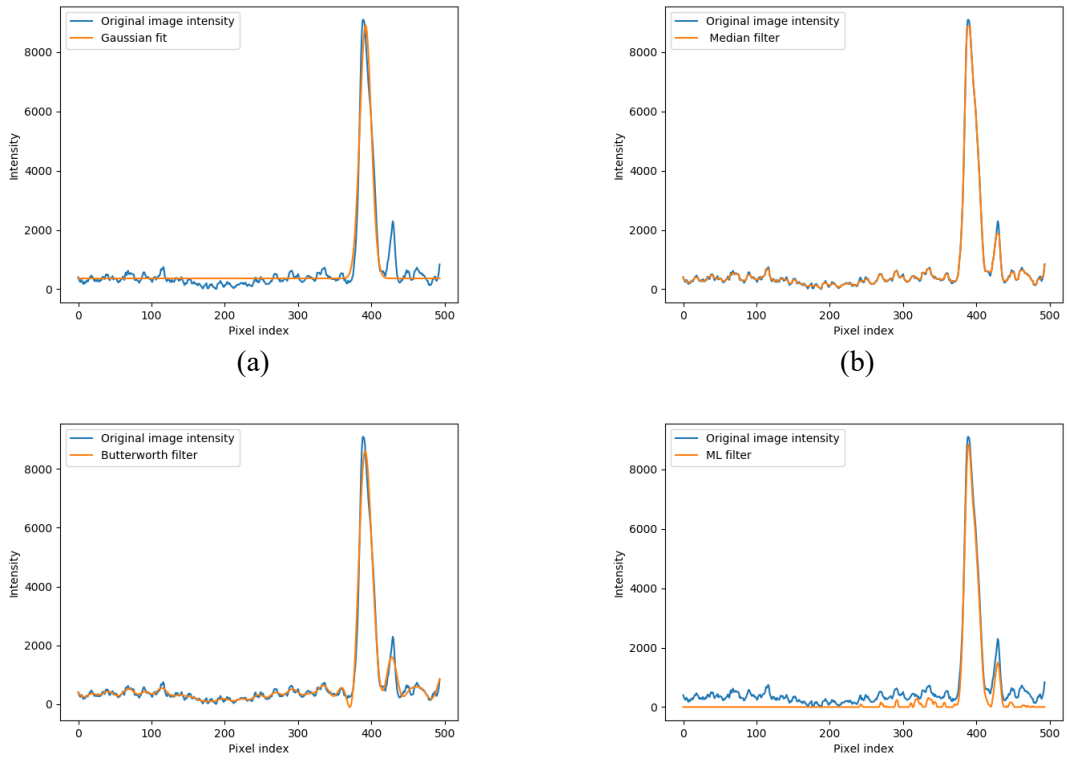

FIG. 8. One example of the comparison with different filters. (a) is Gaussian fitting; (b) is median filter with window length of seven; (c) is 5th order Butterworth filter and critical frequency of 0.09; (d) is ML filter.

Although the ML filter can reduce noise efficiently, the noise from dark current will influence the beamlet position and the RMS size calculation. The slit-scan can be done twice to mitigate this influence to some extent. The first scan is to measure the background from dark current, and the second scan includes beam and dark current. After subtracting the background, the further calculation of the beamlet center and RMS size are done twice. The first is by using the profile of the beamlet image. Then in the second calculation, only intensities in a certain range, beamlet center minus and plus f times RMS size from the first calculation, $[x_c - f\sigma_1, x_c + f\sigma_1]$, are considered. Usually, f is chosen between 0.5 to 5 depending on different image conditions. Fig. 9 and Tab. 1 show an example calculated with different f factors, which indicates that the beamlet RMS size is more sensitive to the value than the center position.

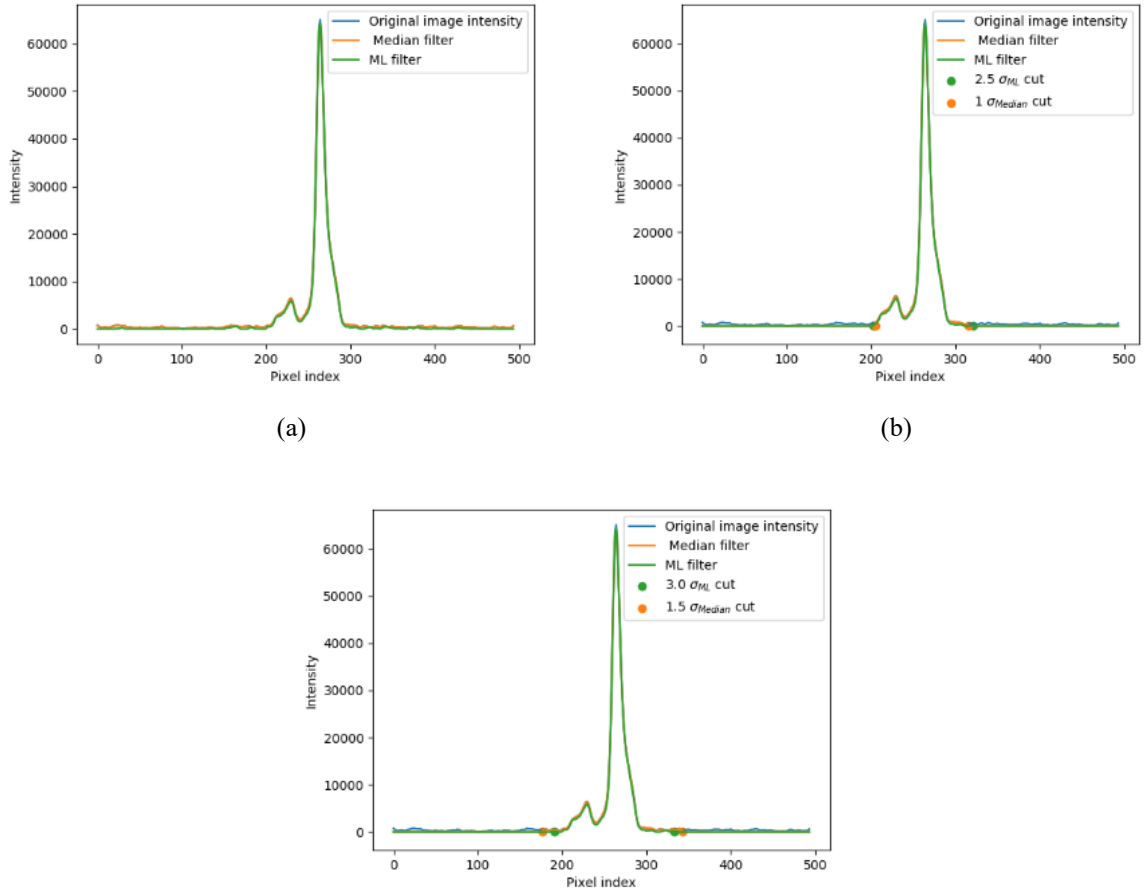

FIG. 9. One example with different cutting factors.

TAB. 1. Beamlets center, RMS size and intensity details of Fig. 10.

ML filter			Median filter		
Limit f	Center (pixel)	RMS size (pixel)	Limit f	Center (pixel)	RMS size (pixel)
no[1]	262.80	23.64	no[1]	260.58	55.07
2.5	262.40	15.36	1	262.29	16.15
3.0	262.50	15.71	1.5	262.31	19.29

4. Emittance correction factor and error analysis

4.1. Emittance correction factor

The beam RMS size can also be measured directly using the YAG screen at slit position. Measurement results showed that the reconstructed beam sizes obtained from the beamlet measurements are mostly smaller than the beam size directly measured on the screen at the slit position. The reason is the finite signal-to-noise ratio which causes signal losses at the low-

[1] means using the whole profile of the beamlet.

intensity edges of the beamlets. This effect has been identified for the first time at the PITZ photo injector [25], and a correction factor f_c has been introduced:

$$f_c = \frac{\sigma_x}{\sqrt{\langle x^2 \rangle}}, \tag{8}$$

where σ_x is the beam RMS size measured at slit position, and $\langle x^2 \rangle$ is the second central moment of the beam distribution as determined by the slits-can measurement. Then the corrected normalized emittance can be written as

$$\varepsilon_n = \frac{\sigma_x}{\sqrt{\langle x^2 \rangle}} \frac{p_z}{m_0 c} \sqrt{\langle x^2 \rangle \langle x'^2 \rangle - \langle x x' \rangle^2}. \tag{9}$$

This conservative approach of the slit-scan analysis has been used in this paper and belongs to the standard slit-scan procedure at the ELBE SRF gun beamline. Fig. 10 shows the correction factor as a function of the bunch charge. For low bunch charges, the factor is in some cases smaller than one. The reason is the dark current or image noise, which is not subtracted from the signal completely, and by that enlarging the reconstructed beam RMS size. In most cases, the factor is between 1.0 and 1.1, especially for higher bunch charges.

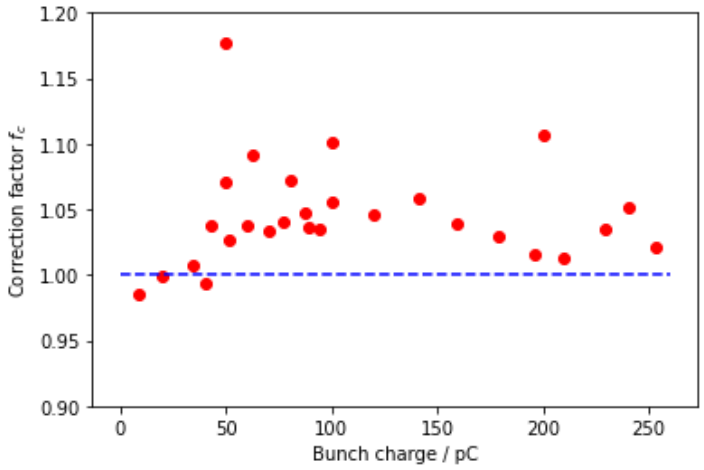

FIG. 10. Correction factor versus bunch charge. The blue dash line is equal to one and the red dots are the correction factors calculated from the slit-scan experiment at different bunch charges.

4.2. Error analysis

The accuracy of slit-scan emittance measurement is mainly determined by four sources: space charge influence in the beamlets (e_1), slit position recording error (e_2), uncertainties in the determination of the beamlet center position and RMS size (e_3), beam energy measurement uncertainly (e_4). The total relative error can be written as:

$$e_t = \sqrt{e_1^2 + e_2^2 + e_3^2 + e_4^2} \tag{10}$$

Although the beam is divided into small slices which reduce the space charge force outside the slit width of the beam, if the beam density is large or the slit width is large, the beamlets may suffer from space charge force in the drift. Ref. [26] introduced a parameter based on the beam transverse envelope equation to evaluate the influence of the space charge force in slit-scan emittance measurements. Assuming that the beam distribution at the slit position is uniform and the slit width is d, the beamlet space charge dominance ratio is given by

$$R_b = \sqrt{\frac{2}{3\pi}} \frac{I}{\gamma I_0} \left(\frac{d}{\varepsilon_n}\right)^2 . \tag{11}$$

In this equation, ε_n is the normalized beam emittance, I is the beam peak current, and γ is the Lorentz factor representing the beam energy and I_0 gives the characteristic current as ec/r_e. When $R_b \ll 1$, the beamlet is emittance dominated and the influence of space charge is negligible. To evaluate the magnitude of the error from space charge, we have done some series of slit-scan simulations considering the influence of the drift distance and space charge. In the simulation, the slit width is 100 μm and the step width is fixed as 100 μm, which can cover all beam without overlap. From the simulation results, the space charge and the drift distance cause errors in the emittance. Generally, when $R_b \leq 0.1$ and the drift distance is larger than 0.5 m, the error is less than 3% and will decrease with enlarging the drift distance, which is independent of space charge. For $R_b > 0.1$, the error from space charge increases with the drift distance enlarge, especially for large R_b, as shown in Fig. 11 (c).

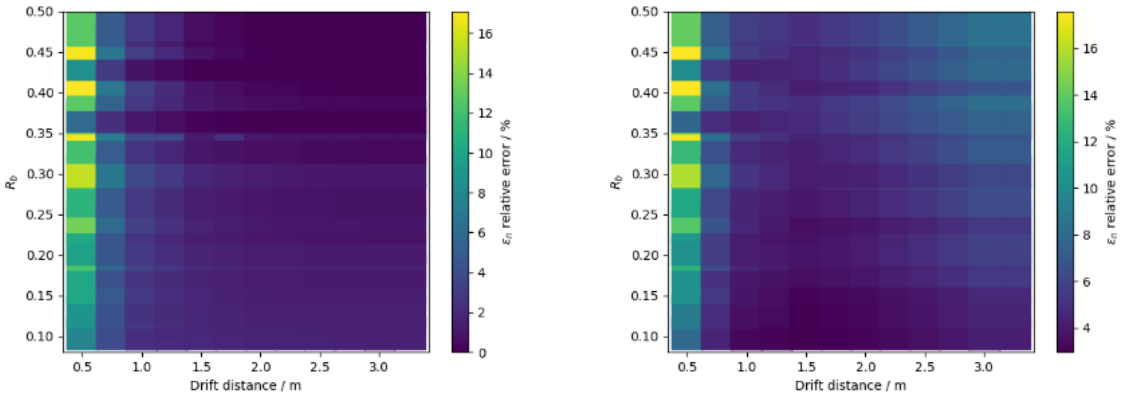

(a) (b)

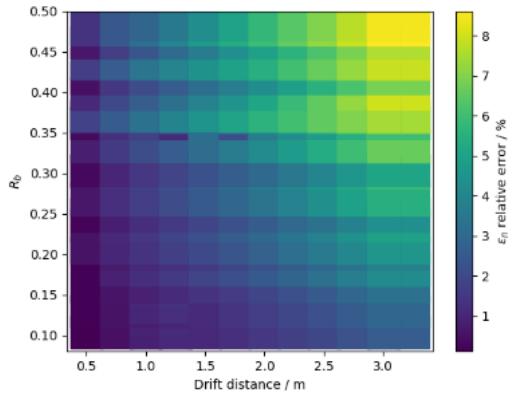

(c)

FIG. 11. Slit-scan simulations: (a) without space charge, (b) with space charge, (c) pure space charge, from (b) subtracts (a).

However, R_b is related to beam current and emittance, which is from the bunch charge, length and horizontal size. In the simulations, we have changed the laser power, laser spot size on the cathode, gun phase and solenoid current that all determine the aforementioned beam parameters. Fig. 12 shows how R_b evolves with bunch charge for laser spot radii on the cathode of 1.25 mm and 1.875 mm. R_b at smaller laser spot radius on the cathode is larger than the bigger one for bunch charge less than 75 pC. For high bunch charge, larger than 100 pC, the smaller laser spot on the cathode has smaller R_b. When R_b is less than 0.5, the error is less than 10% at drift distance of 0.75 m from Fig. 11 (b).

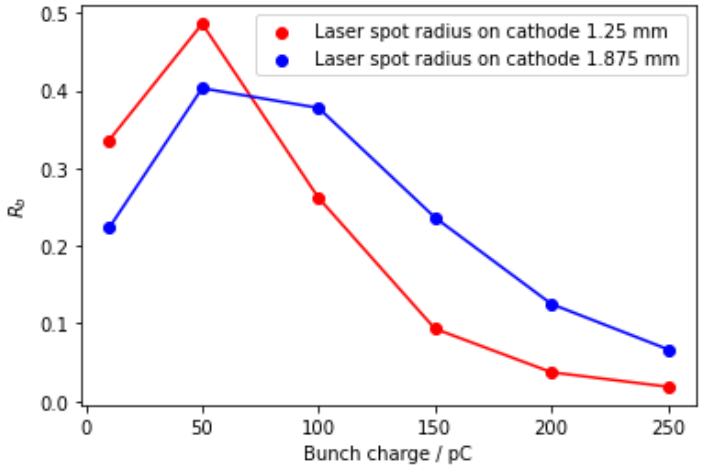

FIG. 12. R_b versus bunch charge for two different laser spot radii on the cathode.

In our equipment, the slit position recording uncertainty is less than 0.6% in average and the energy uncertainty is about 2%. These two factors are linear with the corresponding emittance relative error. Assume the averaged relative uncertainties of the beamlet intensity δ_n, the center position δ_c and the square of RMS size δ_σ, if they are independent for all beamlets and ignore the second and high order terms, the emittance relative error from these can be written as:

$$e_3 \approx \left|\delta_c + \delta_n + \frac{\delta_\sigma}{2}\right|. \quad (12)$$

The details about the derivation of this term are given in the Appendix A.

5. Experiment results

The experiments were carried out with beams of different bunch charges. The SRF gun gradient was set as 8.0 MV/m with a RF launch phase of 55°. The total energy of the beam was 4.45 MeV. As discussed in the former section, to subtract the dark current, every slit-scan was repeated twice where one was without beam and the other one was with beam with the aim to subtract the dark current. The total measurement time was one and a half minutes. Tab. 2 shows the comparison of measurement results and the simulation. The errors are also list inside. The correction factor f_c was calculated by Eq. (8) and the influence of space charge, e_1, was taken from the slit-scan simulation. The slit position uncertainty from the motor system was 0.2 %. The beamlet image intensity, center and RMS size uncertainties were mainly from the system jitter and image noise. In reality, the beamlet from the beam center was to be an evaluation of average of the whole beamlets. Fig.13 shows examples of beamlet intensity, center and RMS size fluctuations at the screen position. The energy uncertainty was around 2 % in our facility due to magnet calibration and RF launch phase drift. The total error, e_t, is calculated by Eq. (8). The normalized emittance for different bunch charges is shown in Fig. 14.

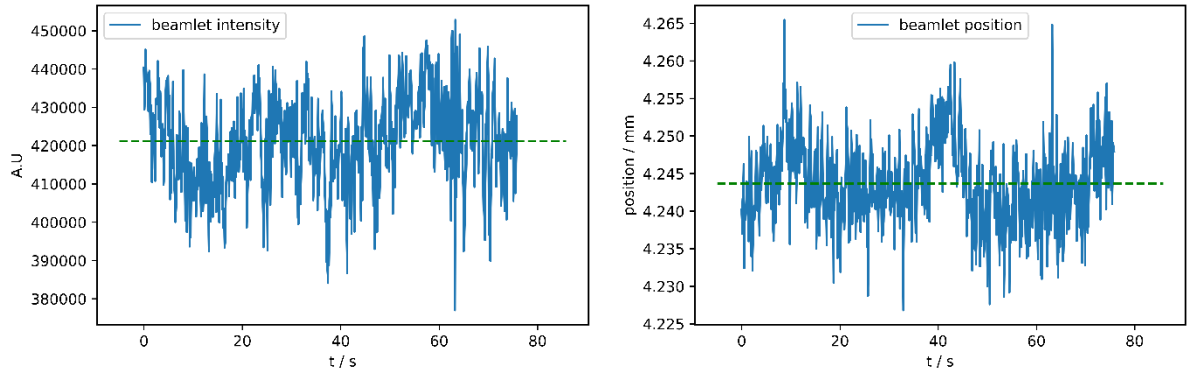

(a) (b)

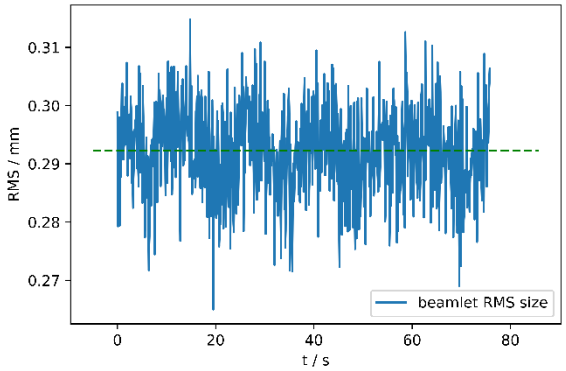

(c)

FIG. 13. Beamlet intensity, center and RMS size uncertainties. The green dash line is the average. The bunch charge is 50 pC and the beamlet is from the center of the beam. The uncertainties of beamlet intensity, center and RMS size are about 2.9%, 0.9% and 10%.

TAB. 2. Examples of measured normalized emittances, beam size correction factors f_c with ML filter, $f_{c,t}$ with traditional filter, charge percent and errors. σ_s and σ_e mean the beam RMS size at slit position in simulation and experiment. $\varepsilon_{n,s}$, $\varepsilon_{n,em}$ and $\varepsilon_{n,et}$ are the beam normalized emittance from the simulation, experiment with processing of ML filter and traditional filter, respectively.

Q (pC)	20	100	120	196	253
f_c	1.00	1.06	1.10	1.01	1.02
$f_{c,t}$	1.03	1.08	1.11	1.02	1.07
Charge percent	0.893	0.935	0.953	0.958	0.948
e_1 (%)	5	8	6	3	0
e_2 (%)	0.2	0.2	0.2	0.2	0.2
e_3 (%)	3.7	5	4.9	2.5	2.5
e_4 (%)	2	2	2	2	2
e_t (%)	6.54	9.64	8.00	4.39	3.21
σ_s (mm)	0.83	0.99	1.14	1.58	1.77
σ_e (mm)	0.93	1.28	1.46	1.64	1.73
$\varepsilon_{n,s}$ (mm·mrad)	1.46	2.84	3.10	4.55	6.04
$\varepsilon_{n,em}$ (mm·mrad)	1.80	3.65	3.42	5.12	6.19
$\varepsilon_{n,et}$ (mm·mrad)	2.5	4.92	4.12	5.23	6.37

As a comparison with normalized emittance from experiments, ASTRA simulations with different bunch charges were performed. The initial spatial beam distribution at the cathode is defined by two effects, the QE distribution of the cathode and the transversal intensity distribution of the laser. Two different emission conditions of the cathode have been appeared in the experiments, and are shown in Fig. 15. In the first row of Fig. 15, (a) shows an inhomogeneous QE map of the cathode. With the laser of 3.75 mm diameter with uniform distribution shown in (b), it generates a beam distribution as in (c), which is applied in the simulation with the results showing the red line in Fig. 14. With a smaller laser spot diameter of 2.5 mm, the homogenous part of the QE distribution could be selected and it produces a beam with Gaussian distribution like in Fig. 15 (f). In Fig. 14, the green line presents the emittance results of this situation. Fig. 15 (d) shows a well-distributed QE mapping from the experiment.

Together with a homogenous laser shape as in Fig. 15 (e), the beam at the cathode has then a Gaussian distribution. The cyan line in Fig. 14 is the result from this simulation with a Gaussian distribution beam. In simulation and experiments the temporal distribution of the laser was Gaussian with 2.3 ps RMS pulse length. The difference between the measurement results and the simulation is from the optical aberration, such as multipole fields parasitic in the solenoid or cavity [27]. Although we have installed the corrector including a normal quadrupole and a skew quadrupole, the influence of the unusual fields on the beam cannot be canceled totally.

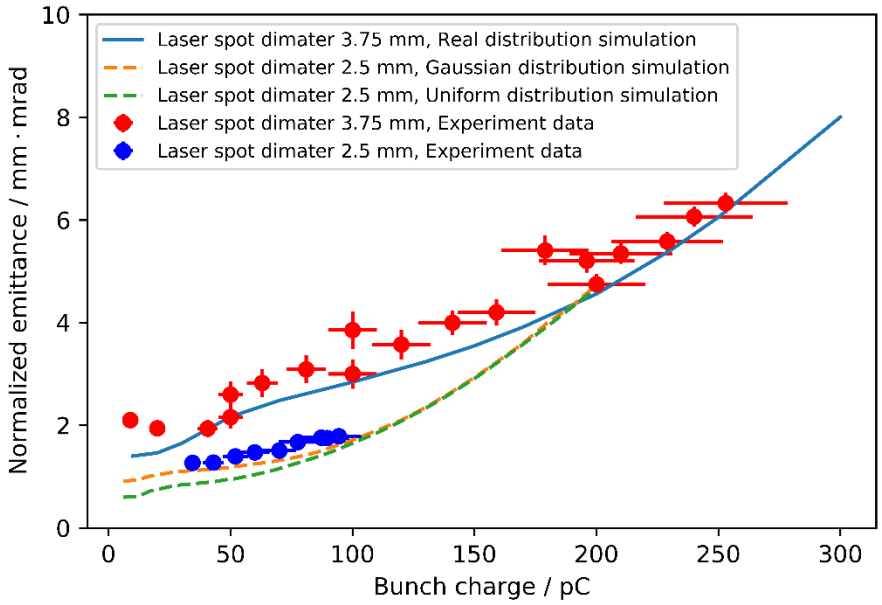

FIG. 14. Normalized emittance for varied bunch charges obtained from simulations and experiments with different spatial particle distributions at the cathode.

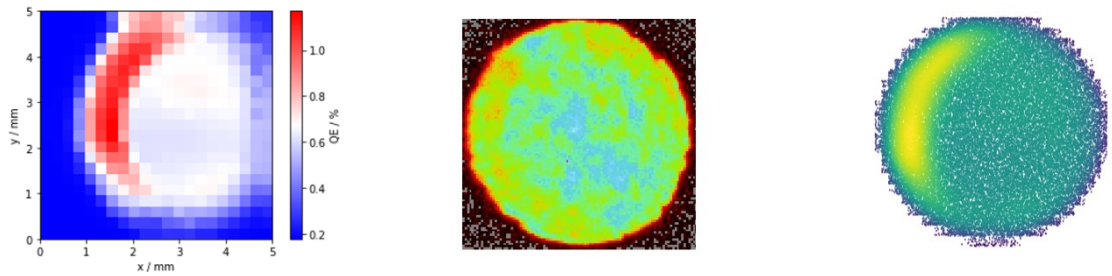

(a) (b) (c)

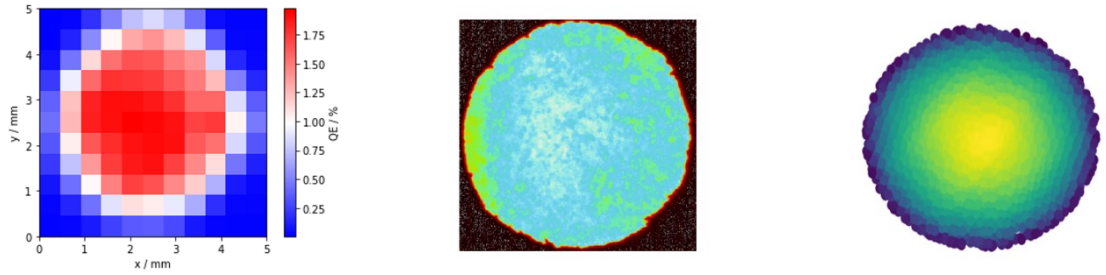

(d) (e) (f)

FIG. 15. (a) and (d) are the QE maps, (b) and (e) are the laser spot distributions on virtual cathode, (c) and (e) are original particles distributions in simulation. (c) is the inhomogeneous distribution and (f) is the gaussian distribution.

6. Conclusions

To improve the speed and the accuracy of the slit-scan emittance measurement at the ELBE SRF gun beamline, we constructed a new fast slit-scan system with a fast and continuous moving motor. Meanwhile, we have introduced two machine learning algorithms, the CNN for classification and the encoder-decoder CNN for filtering noise to shorten the image processing time. The ML filter is potentially more effective than the traditional imaging processing methods for beamlet images. The systematic errors from the slit moving and the image processing were attentively analyzed. At the end, the experimental measurement results were compared with the ASTRA simulations. The results confirmed the accuracy of the new slit-scan system besides the significant improvement of measurement speed.

Acknowledgement

We would like to thank the whole ELBE team for their help with the experiments. We also thank Dr. Houjun Qian from PITZ, DESY for his constructive discussions. This work was supported by China Scholarship Council and Chinese Academy of Engineering Physics. The machine learning part is supported by Helmholtz Information & Data Science Academy (HIDA) (No. 11952).

References

[1] T. Rao and D. H. Dowell, An engineering guide to photoinjectors, arXiv:1403.7539 (2014).

[2] I. Grguraš, A. R. Maier, C. Behrens, et al. Ultrafast X-ray pulse characterization at free-electron lasers, Nature Photonics, 6(12): 852-857, 2012.

[3] S. Serkez, G. Geloni, S. Tomin, et al. Overview of options for generating high-brightness attosecond x-ray pulses at free-electron lasers and applications at the European XFEL, Journal of Optics, 20(2): 024005, 2018.

[4] C. Pellegrini, X-ray free-electron lasers: from dreams to reality, Physica Scripta 2016, 014004 (2017).

[5] L. Merminga, Energy recovery linacs, Synchrotron Light Sources and Free-Electron Lasers: Accelerator Physics, Instrumentation and Science Applications, 439-477, 2020.

[6] S. Wethersby, G. Brown, M. Centurion, T. Chase, R. Coffee, J. Corbett, J. Eichner, J. Frisch, A. Fry, M. Gühr, et al., Mega-electron-volt ultrafast electron diffraction at SLAC National Accelerator Laboratory, Review of Scientific Instruments 86, 073702 (2015).

[7] D. Kayran, Z. Altinbas, D. Bruno, M.R. Constanzo, A. Drees, A. V. Fedotov, W. Fischer, M. Gaowei, D. W. Gassner, X. Gu et al., High-brightness electron beams for linac-based bunched beam electron cooling, Phys. Rev. Acc. and Beams, 23, 021003 (2020).

[8] C. Lejeune and J. Aubert, Emittance and Brightness: Definitions and Measurements in Applied Charged Particle Optics, Part A, edited by A. Septier (Academic Press, New York, 1980), p. 159 .

[9] J. D. Lawson, The Physics of Charged Particle Beams (Clarendon Press, Oxford, 1988), p. 156

[10] P. M. Lapostolle, Possible emittance increase through filamentation due to space charge in continuous beams, CERN Report ISR/DI-70-36 (1970); IEEE Trans. Nucl. Sci. NS-18, 1101 (1971).

[11] F. J. Sacherer, RMS envelope equations with space charge, IEEE Trans. Nucl. Sci. NS-18, 1105 (1971).

[12] E. Prat, M. Aiba, Four-dimensional transverse beam matrix measurement using the multiple-quadrupole scan technique. Phys. Rev. ST Accel. Beams 17, 052801 (2014).

[13] H. Wiedemann, Particle Accelerator Physics (Springer Publishing, 2015) p. 224.

[14] K. M. Hock, M.G. Ibison, D. J. Holder, B.D. Muratori, A. Wolski, G. Kourkafas, B. J. A. Shepherd, Beam tomography research at Daresbury Laboratory. Nucl. Instrum. and Methods A 753, 38 (2014).

[15] M. Zhang, Emittance formula for slits and pepper-pot measurement, FERMILAB-TM-1988, Fermilab 1996.

[16] S. G. Anderson, J. B. Rosenzweig, G. P. LeSage, and J. K. Crane, Space-charge effects in high brightness electron beam emittance measurements, Phys. Rev. ST Accel. Beams 5, 014201 (2002).

[17] P. Michel, ELBE Center for high-power radiation sources, J. Large-Scale Res. Facil. 2, A39 (2016); https://www.hzdr.de/db/Cms?pNid=145.

[18] J. Teichert, A. Arnold, G. Ciovati, J.-C. Deinert, P. Evtushenko, M. Justus, et al., Successful user operation of a superconducting radio-frequency photoelectron gun with Mg cathodes, Phys. Rev. Accel. Beams 24, 033401 (2021).

[19] S. Indolia, A. K. Goswami, S. P. Mishra, and P. Asopa, Conceptual understanding of convolutional neural network-a deep learning approach. Procedia computer science, 132: 679-688 (2018).

[20] J. Zhu, Y. Chen, F. Brinker, W. Decking, S. Tomin, and H. Schlarb, High-fidelity prediction of megapixel longitudinal phase-space images of electron beams using encoder-decoder neural networks, Physical Review Applied, 16(2): 024005 (2021).

[21] D. P. Kingma, M. Welling, An introduction to variational autoencoders. arXiv preprint arXiv:1906.02691 (2019).

[22] K. Floettmann, A Space Charge Tracking Algorithm (ASTRA), http://www.desy.de/mpyflo (2007).

[23] K. P. Murphy, Machine learning: a probabilistic perspective (MIT press, 2012) p.54.

[24] A. Paszke, S. Gross, F. Massa, A. Lerer, Bradbury, Chanan G, et al. PyTorch: An Imperative Style, High-Performance Deep Learning Library. In: Advances in Neural Information Processing Systems 32 [Internet]. Curran Associates, Inc.; 2019. p. 8024–35. Available from: http://papers.neurips.cc/paper/9015-pytorch-an-imperative-style-high-performance-deep-learning-library.pdf

[25] H. J. Qian, M. Krasilnikov, Z. Aboulbanine, et al. Analysis of photoinjector transverse phase space in action and phase coordinates. Phys. Rev. Accel. Beams 25, 103401 (2022).

[26] S. G. Anderson, J. B. Rosenzweig, G. P. LeSage, J. K. Crane. Space-charge effects in high brightness electron beam emittance measurements. Phys. Rev. Accel. Beams, 5(1): 014201 (2002).

[27] D. H. Dowell, F. Zhou, and J. Schmerge, Exact cancellation of emittance growth due to coupled transverse dynamics in solenoids and rf couplers, Phys. Rev. Accel. Beams 21, 010101 (2018).

Appendix A

Consider the averaged relative uncertainties of the beamlet intensity δ_n, the center position δ_c and the square of RMS size δ_σ. Assuming that they are independent for all beamlets, the i-th beamlet intensity, center and square RMS size can be written as

$$n_{i,r} = (1 \pm \delta_n) n_i, \tag{A. 1}$$

$$\overline{x}_{sci,r} = (1 \pm \delta_c) \overline{x}_{sci}, \tag{A. 2}$$

$$\sigma_{i,r}^2 = (1 \pm \delta_\sigma) \sigma_i^2, \tag{A. 3}$$

where $\overline{x}_{sci,r}$ is the real center of the i-th beamlet on the screen. From these equations, $\langle x^2 \rangle_r$, $\langle x'^2 \rangle_r$ and $\langle x x' \rangle_r$ can be derived if we ignore higher order error terms:

$$\langle x^2 \rangle_r = \langle x^2 \rangle \pm \delta_n \langle x^2 \rangle \,, \tag{A. 4}$$

$$\langle x'^2 \rangle_r = \langle x'^2 \rangle \pm \frac{2\delta_c}{L} \langle x' \overline{x}_{sc} \rangle \pm \delta_\sigma \langle \sigma'^2 \rangle \pm \delta_n \langle x'^2 \rangle \,, \tag{A. 5}$$

$$\langle x x' \rangle_r = \langle x x' \rangle \pm \frac{\delta_c}{L} \langle x_s \overline{x}_{sc} \rangle \pm \delta_n \langle x x' \rangle. \tag{A. 6}$$

From the equations above, it can be seen that coordinate systems of the slit and screen position cross each other, when the beamlet center has an error. Ignoring higher orders of δ_n, δ_c, δ_σ, the calculated geometric emittance is

$$\varepsilon_c^2 \approx \varepsilon_0^2 \pm \frac{2\delta_c}{L} (\langle x^2 \rangle \langle x' \overline{x}_{sc} \rangle - \langle x x' \rangle \langle x_s \overline{x}_{sc} \rangle) \pm \delta_\sigma \langle \sigma'^2 \rangle \langle x^2 \rangle \pm 2\delta_n \varepsilon_0^2. \tag{A. 7}$$

Introducing

$$\frac{\langle x^2 \rangle \langle x' \overline{x}_{sc} \rangle - \langle x x' \rangle \langle x_s \overline{x}_{sc} \rangle}{L} = k_c \varepsilon_0^2 \,, \tag{A. 8}$$

$$\langle \sigma'^2 \rangle \langle x^2 \rangle = k_\sigma \varepsilon_0^2 \,, \tag{A. 9}$$

then the emittance error from these uncertainties has the form

$$e_3 = \frac{|\varepsilon_c - \varepsilon_0|}{\varepsilon_0} \approx \left| \sqrt{1 \pm 2\delta_c k_c \pm 2\delta_n \pm \delta_\sigma k_\sigma} - 1 \right| \approx \left| \delta_c k_c + \delta_n + \frac{\delta_\sigma k_\sigma}{2} \right|, \tag{A. 10}$$

Note that k_c and k_σ depend on the distribution of the beam in phase space and on the relationship of the coordinate systems at the slit and screen position. Practically it is difficult to calculate them because they include the geometric emittance true values. Here we estimate them to be the same magnitude as the true emittance and be one. By this simplification, the error from beamlet intensity, center position as well as RMS size uncertainties is written as $\left| \delta_n + \delta_c + \frac{\delta_\sigma}{2} \right|$.